ORIGINAL PAPER

Peroxidase-mimicking nanozyme with surface-dispersed Pt atoms for the colorimetric lateral flow immunoassay of C-reactive protein

Vasily G. Panferov[1] · Nadezhda A. Byzova[1] · Anatoly V. Zherdev[1] · Boris B. Dzantiev[1]

Abstract

Platinum-containing nanozymes with peroxidase-mimicking activity (PMA) have found a broad application in bioanalytical methods and are potentially able to compete with enzymes as the labels. However, traditionally used methods for the synthesis of nanozymes result in only a small fraction of surface-exposed Pt atoms, which participate in catalysis. To overcome this limitation, we propose a new approach for the synthesis of nanozymes with the efficient dispersion of Pt atoms on particles' surfaces. The synthesis of nanozymes includes three steps: the synthesis of gold nanoparticles (Au NPs), the overgrowth of a silver layer over Au NPs (Au@Ag NPs, 6 types of NPs with different thicknesses of Ag shell), and the galvanic replacement of silver with $PtCl_6^{2-}$ leading to the formation of trimetallic Au@Ag-Pt NPs with uniformly deposited catalytic sites and high Pt-utilization efficiency. Au@Ag-Pt NPs (23 types of NPs with different concentrations of Pt) with various sizes, morphology, optical properties, and PMA were synthesized and comparatively tested. Using energy-dispersive spectroscopy mapping, we confirm the formation of core@shell Au@Ag NPs and dispersion of surface-exposed Pt. The selected Au@Ag-Pt NPs were conjugated with monoclonal antibodies and used as the colorimetric and catalytic labels in lateral flow immunoassay of the inflammation biomarker: C-reactive protein (CRP). The colorimetric signal enhancement was achieved by the oxidation of 3,3′-diaminobenzidine by H_2O_2 catalyzed by Au@Ag-Pt NPs directly on the test strip. The use of Au@Ag-Pt NPs as the catalytic label produces a 65-fold lower limit of CRP detection in serum (15 pg mL^{-1}) compared with Au NPs and ensures the lowest limit of detection for equipment-free lateral flow immunoassays. The assay shows a high correlation with data of enzyme-linked immunosorbent assay ($R^2 = 0.986$) and high recovery (83.7–116.2%) in serum and plasma. The assay retains all the benefits of lateral flow immunoassay as a point-of-care method.

Introduction

Nanoparticles (NPs) with enzyme-mimicking activities (nanozymes) consisting of noble metals have found a broad application as the signal-generator label in different assays [1]. Among them, platinum-containing nanozymes demonstrate high peroxidase- and catalase-mimicking activities and remarkable stability in extremal ranges of pH, temperatures, and concentrations of inhibitors [2, 3]. The combination of

these features with unique physicochemical properties arising from nanoscale size and chemical composition (i.e., the high surface area for conjugation with receptor biomolecules, high molar extinction coefficient) makes Pt-containing nanozymes a promising alternative to natural peroxidases as well as a multifunctional analytical tool [4].

However, the high consumption of precious Pt precursors for the synthesis of nanozymes remains a significant limiting factor for routine use. Thus, the new approaches for the synthesis of nanomaterials with high catalytic activity and low precursor consumption are in great demand [5]. Conventional methods of Pt-nanozyme synthesis (reduction of precursor or layer-by-layer growth) lead to the formation of NPs in which the major number of atoms are buried inside the particle and do not participate in catalysis (i.e., calculations show that for 20 nm spherical Au NPs, only about 5% of all atoms are surface-exposed) [6, 7]. The

✉ Boris B. Dzantiev
dzantiev@inbi.ras.ru

1   A.N. Bach Institute of Biochemistry, Federal Research Centre "Fundamentals of Biotechnology", Russian Academy of Sciences, Leninsky Prospect 33, 119071 Moscow, Russia

exposure of a maximal number of Pt atoms on the NP's surface will facilitate high peroxidase-mimicking activity (PMA) and low consumption of the precious precursor.

At the moment, there are few approaches to synthesizing nanozymes with high PMA and low consumption of Pt precursors: the reduction of the nanozymes' sizes to the structures consisting of dozens of metal atoms (nanoclusters) [8], the formation of hollow nanoparticles [9], and the formation of close-to-monolayer catalytic-active sites [10] or even atomic dispersion of active sites (single-atom catalyst) on the support [11]. The first two approaches aim to maximize the surface/volume (mass) ratio and to increase the number of surface-exposed Pt atoms. However, sophisticated preparations, low colorimetric signals, and the low number of sites for bioconjugation are the major drawbacks of these NPs. The elegant method for the efficient dispersion of Pt atoms on the surface of Au NPs was demonstrated by Gao et al. [10]. The authors maintain the conditions (i.e., precursor injection rate) that provide a higher rate of the surface diffusion of Pt atoms than the rate of their deposition by the reduction. Thus, the Pt atoms spread across the Au surface and facilitate smooth Pt coverage with an adjustable thickness (1–10 layers). The applicability of the approach of precise control over deposition and diffusion rates was proven by the conformal coating of Pd NPs with Ru [12] and Ir [13], which demonstrated superior catalytic activities.

In this article, we propose the easy hydrothermal synthesis of trimetallic nanozyme with high PMA and low consumption of Pt precursor. The synthesis of trimetallic nanozymes includes three consistent steps. In the first step, Au NPs are synthesized by the reduction of $HAuCl_4$ with sodium citrate. In the next step, $AgNO_3$ is reduced by ascorbate in the presence of Au NPs, acting as the seeds with the formation of core@shell Au@Ag NPs [14]. In the third step, deposition of Pt is performed by the reaction of galvanic replacement: spontaneous electrochemical reactions driven by the difference of reduction potentials between Ag in Au@Ag NPs and $PtCl_6^{2-}$ in solution [15]. As a result of this process, the oxidation of Ag is accompanied by the reduction of ions from the solution and the Pt deposition on the NPs. The oxidation of the Ag atoms (as well as the reduction and deposition of Pt) is started on the surface [16, 17] and then continued within a particle through the formation of pinholes, resulting in the formation of hollow nanoparticles [18].

The reactions occur on the solvent-exposed sites and, as we hypothesize, will facilitate the higher number of the surface-exposed Pt atoms in comparison with conventional spherical nanoparticles. Although the used approaches of the syntheses (i.e., overgrowth, galvanic replacement) are well-known, their usefulness for the synthesis of trimetallic NPs with high PMA and low consumption of Pt precursor was demonstrated for the first time. In the previous articles, nanozymes containing the same chemical composition but a different distribution of

metals (core@shell@shell NPs – Au@Ag@Pt) were reported as the label in lateral flow immunoassay (LFIA) [19] and an enzyme-linked immunosorbent assay (ELISA)–like method [20]. Au@Ag@Pt NPs were synthesized by the consistent two-stage in situ reduction of Ag and Pt on seed NPs with the formation of Au@Ag and Au@Ag@Pt NPs. Although this approach results in the formation of unblocked Pt surface, layer-by-layer growth of Pt does not provide an optimal distribution of atoms and leads to the high consumption of Pt precursor. Thus, the proposed in this article approach of Pt distribution in Au@Ag-Pt NPs and the use of these NPs as the label are novel.

To fully realize the potential of nanozymes as the optical and catalytic label, we used Au@Ag-Pt NPs as the label in LFIA. LFIA is based on the formation of immune complexes between antibodies and antigens during the migration of the liquid sample along the porous membrane with immobilized immunoreagents [21]. Nanozymes conjugated with antibodies act as the colorimetric label, and they facilitate the visual detection of immune complexes captured by antibodies immobilized in a membrane's test zone. If the target's concentration is low, then the minimal number of nanozymes is captured in the test zone, and a colorimetric signal is weak. A post-assay increase of the colorimetric signal is achieved by the accumulation of the product catalyzed by the nanozyme directly on the membrane [22]. Because LFIA is a routinely used point-of-care method, the low consumption of precious Pt precursors is especially in demand.

As the target analyte, we used C-reactive protein (CRP): the acute-phase inflammation biomarker widely controlled in routine clinical practice. The highly sensitive detection and the control of the dynamics of the CRP level in a broad range of concentrations are a necessary part of diagnostics and monitoring for therapy efficiency [23]. Social request for rapid, highly sensitive, and reliable methods for routine monitoring of biomarkers' levels [24] determines great demand of the present development.

Materials and methods

Materials

Native human CRP and two clones of monoclonal antibodies (mAb) against CRP (C2cc and C6cc clones) were purchased from HyTest (Moscow, Russia, www.hytest.fi). Goat antimouse antibodies were purchased from Arista Biologicals (Allentown, USA, www.aristabiologicals.com). Lyophilized human serum (TruLab N) was purchased from DiaSys (Holzheim, Germany, www.diasys-diagnostics.com). Human serum and plasma were kindly provided by N. I. Pirogov City Clinical Hospital No. 1 (Moscow, Russia, www.gkb1.ru) and collected from volunteers and patients after obtaining written and informed consent. Rabbit serum

was obtained by centrifugation (10 min, 4000 g) from blood after coagulation (5h at 37°C). Tetrachloroauric (III) acid, sodium hexachloroplatinate (IV), silver nitrate, nickel (II) sulfate hexahydrate, 3,3′-diaminobenzidine (DAB), 3,3′,5,5′-tetramethylbenzidine (TMB), 30% hydrogen peroxide, sodium ascorbate, trisodium citrate, bovine serum albumin (BSA), streptavidin-peroxidase polymer, Au, Ag, and Pt standards for mass spectrometry were purchased from Sigma-Aldrich (St. Louis, USA, www.sigmaaldrich.com). All salts, acids, alkalis, and solvents were purchased from Chimmed (Moscow, Russia, www.chimmed.ru). ELISA was performed using polystyrene microplates 9018 provided by Corning Costar (Tewksbury, USA, www.corning.com). Lateral flow test strips were fabricated using nitrocellulose membranes CNPC-12, fiberglass conjugate release matrix PT-R5, and sample (GFB-R4) and absorbent (AP045) pads from Advanced Microdevices (Ambala Cantt, India, www.mdimembrane.com).

Apparatus

For the separation of nanoparticles, an Eppendorf centrifuge 5430 was used. The optical measurements were performed using the cuvette spectrophotometer Biochrom Libra S80 (Cambridge, UK, www.biochrom.co.uk) and the multifunctional plate reader PerkinElmer EnSpire Multimode Plate Reader (Waltham, USA, www.perkinelmer.com). The antibodies were dispensed on the membranes using an Imagene Technology IsoFlow dispenser (Hanover, USA). The guillotine cutter from A-Point Technologies Index Cutter-1 (Gibbstown, USA) was used to prepare the test strips. Digital images of the test strips after assay were obtained using a Canon 9000F Mark II scanner (Tokyo, Japan, www.canon.com). The size and the morphology of the NPs were studied by transmission electron microscopy using the Jeol JEM-1400 microscope (Tokyo, Japan, www.jeol.co.jp). Energy-dispersive spectroscopy (EDS) and EDS mapping were performed using the transmission electron microscope Tecnai Osiris FEI equipped with the Super-X windowless EDX detector system (Hillsboro, USA, www.fei.com). The concentrations of Au, Ag, and Pt in the NPs were measured by inductively coupled plasma-mass spectrometry using the spectrometer Perkin-Elmer ELAN DRC-II (Waltham, USA, www.perkinelmer.com).

Synthesis of Au, Au@Ag, and Au@Ag-Pt NPs

The detailed procedure of Au (one type), Au@Ag (6 types), and Au@Ag-Pt (23 types) NPs' syntheses is described in the Supplementary information. Based on the final concentrations of silver nitrate (shown in brackets), Au@Ag NPs were denoted as Au@Ag #1 NPs (50 μM), Au@Ag #2 NPs (100 μM), Au@Ag #3 NPs (200 μM), Au@Ag #4 NPs (500 μM), Au@Ag #5 NPs (1000 μM), and Au@Ag #6 NPs (1500 μM).

For the synthesis of Au@Ag-Pt NPs, all six types of Au@Ag NPs were used. The final concentrations of Na_2PtCl_6 varied with a range from 8 to 0.12 for the ratio Pt^{4+}/Ag^+ (Table S1).

The mAb (C6cc clone) was conjugated to NPs using physical adsorption method. The detailed procedure is described in the Supplementary information section S1.5.

Test strip preparation

Antimouse IgG (1 mg mL^{-1}) and mAb to CRP (C2cc clone, 1 mg mL^{-1}) in 50 mM of potassium phosphate buffer with 0.05 M of NaCl, pH 7.4 (PBS), were dispensed (0.15 μL mm^{-1}) at the control and test zones (CZ and TZ, respectively) on the nitrocellulose membrane CNPC-12. Fiberglass membrane PT-R5 was soaked (1.5 μL mm^{-1}) with NP conjugates (OD$_{\lambda max}$ = 4.0). All membranes were dried at 30°C for 24 h; then, the sample and the absorbent pads were glued. After cutting, the test strips were stored in zip pockets at room temperature.

Lateral flow immunoassay

Four formats of LFIA were performed using different NPs as the label: that is, Au NPs (LFIA-1), Au@Ag NPs (LFIA-2), Au@Ag-Pt NPs acting as the colorimetric label (LFIA-3), and Au@Ag-Pt NPs acting as the label with PMA (LFIA-4). All four formats were performed following the same procedure. For calibration plots, rabbit serum was diluted 4 times with PBST and spiked with CRP (1000–0.004 ng mL^{-1}). For the analysis of real samples, human plasma and serum were diluted (4–200 times) with PBST. The test strips were immersed vertically in the sample (100 μL) and incubated for 5 min. For LFIA-4, a substrate solution (0.05% DAB, 200 mM H_2O_2, 0.05% NiSO$_4$*7H$_2$O in 50 mM PBS, pH 7.3) was dropped (10 μL) on the test strips after completion of LFIA-3 and incubated for 5 min. The test strips were scanned, and the values of the intensity of coloration of the TZs in the grayscale mode were calculated using TotalLab TL120 software (Nonlinear Dynamics, Newcastle, UK, www.totallab.com). For the calibration plots, each concentration was studied in triplicate. The real samples were studied in duplicate. The limit of detection (LOD) values were determined as the concentration providing a colorimetric signal higher than the sum of the colorimetric signal of the blank probe and its three standard deviations.

Results and discussion

Characterization of Au and Au@Ag nanoparticles

The Au NPs were synthesized using the citrate reduction method. The mean diameter of Au NPs was equal to 17.9 ±

1.4 nm, and no aggregates were observed (Fig. 1a, Fig. S3 a,b). The shape of Au NPs was close to spherical, and the elongation coefficient (ratio of major axis length of the particle to the minor axis length, Table S3) was equal to 1.07 ± 0.07. The results confirm the homogeneity and colloidal stability of Au NPs and their applicability as the seeds for the formation of the silver shell.

The reduction of silver nitrate in the suspension of Au NPs leads to the formation of core@shell Au@Ag NPs (Fig. 1b–c, Fig. S3 c-n). The mean diameters and elongation coefficients of Au@Ag NPs are summarized in Table S3. The formation of the silver layer around Au NPs results in the shift of λmax and the increase of the absorbance value (Fig. S4).

The results of EDS confirm the presence of Ag in the synthesized NPs (Fig. S5). Au@Ag NPs synthesized with the concentration of silver nitrate ≥ 500 μM (Au@Ag #4–6) result in the formation of polydispersed NPs (histograms of the diameter distribution of NPs and TEM microphotographs are presented in Fig. S3 c-n) with nonuniform silver coatings.

The formation of the silver layer was proven by the increase of the hydrodynamic size of NPs (Fig. S6) and EDS mapping of Au@Ag #2 NPs (Fig. 2) and Au@Ag #4 NPs (Fig. S7, 8). Ag atoms are spread over the whole surface of Au NPs (Fig. 2b) and form the shell (Fig. 2c). The relative contents of Au and Ag are dependent on the concentrations of precursors and were equal to 60.2 and 39.8% for Au@Ag #4 NPs and 73.2 and 26.7% for Au@Ag #2 NPs, respectively.

For the deposition of platinum, galvanic replacement was performed for Au@Ag #1, 3, 5, and 6 NPs with an equal ratio of Pt^{4+}/Ag concentrations (Table S1). For Au@Ag #2 and #4 NPs, the influence of different ratios of Pt^{4+}/Ag on the size, optical properties, and morphology of NPs was studied in a broad concentrations ration (Pt^{4+}/Ag within 8–0.07 for Au@Ag #2 NPs and 4–0.005 for Au@Ag #4 NPs, Table S1). The changes of the concentrations of Pt during the galvanic replacement in Au@Ag #2–Pt #1–7 NPs were monitored with ICP-MS (Fig. S9).

The concentrations of Pt in Au@Ag #2–Pt NPs are dependent on the added amount of $PtCl_6^{2-}$ ions only in the area where the ratio of $Pt^{4+}/Ag \leq 1$. Although the added concentrations of Pt for Au@Ag #2–Pt #1–3 were high (20.5 ± 0.3, 10.25 ± 0.17, and 5.13 ± 0.08 mg L^{-1}), the detected concentrations of Pt in Au@Ag #2–Pt #1–3 NPs were significantly lower (2.95 ± 0.06, 2.76 ± 0.06, and 2.17 ± 0.06 mg L^{-1} of Pt, Fig. S9a). This fact confirms the deposition of Pt is performed by galvanic replacement and is thus limited by the concentration of Ag in the Au@Ag #2 NPs. According to ICP-MS measurements, the concentration of Ag in Au@Ag #2 NPs was equal to 5.7 ± 0.2 mg L^{-1}, limiting the maximum predicted amount of deposited platinum to 2.49–2.67 mg L^{-1} (Fig. S9a, the area between red-dotted lines). The excess of the added $PtCl_6^{2-}$ ions is not deposited on the particles because of the absence of the reducing agents. By contrast, the concentrations of Pt in Au@Ag #2–Pt #4–7 NPs (i.e., equal and below the value of the maximum predicted amount of deposited platinum, i.e., $Pt^{4+}/Ag \leq 1$) demonstrated a good correlation with the added concentrations of platinum (Fig. S9b). This proves the deposition of platinum in nanoparticles was achieved by galvanic replacement.

Galvanic replacement results in the change of the NPs' morphology because the replacement of four Ag leads to the addition of the single Pt atoms: $4Ag^0 + PtCl_6^{2-} \rightarrow 4Ag^+ + Pt^0 + 6 Cl^-$. As the galvanic replacement continues, the inequivalent replacement leads to the formation of pinholes, voids, and finally hollow particles. Au@Ag #1–3 NPs have a thin Ag shell, and the galvanic replacement of Ag atoms does not lead to the change of the morphology of NPs (Fig. 3a, Fig. S10 a–j).

The formation of voids after galvanic replacement was observed for only Au@Ag #4–6 NPs (i.e., for NPs with a thick enough Ag shell; Fig. 3b, c, Fig. S10 k–p). The diameter of the intrinsic particles is equal to the initial Au NP, and the size of the voids corresponds to the thickness of the silver layers. Galvanic replacement results in the shift of maximum absorbance wavelength to the long-wave region (Fig. S11). Thus, the formation of Au@Ag-Pt NPs during galvanic replacement
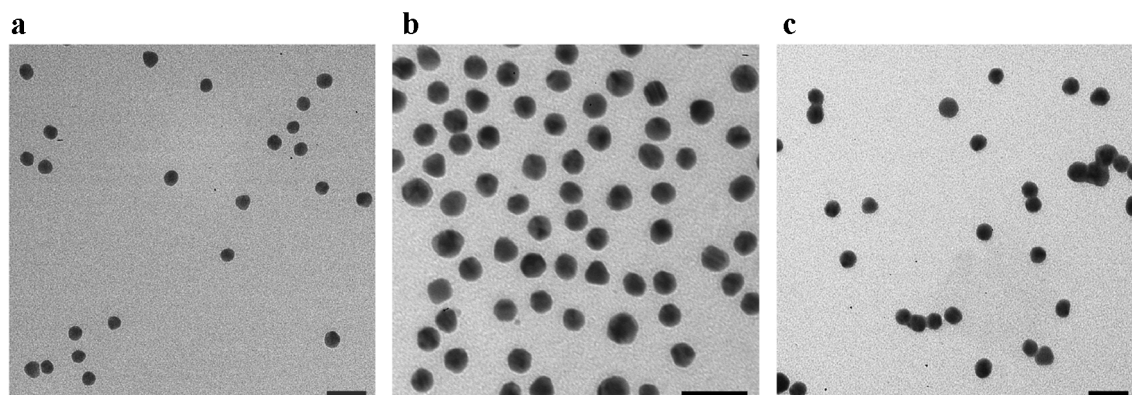
Fig. 1 Characteristics of Au and Au@Ag NPs. TEM microphotographs of Au NPs (**a**), Au@Ag #2 (**b**), and Au@Ag #3 (**c**). The scale bar is equal to 50 nm
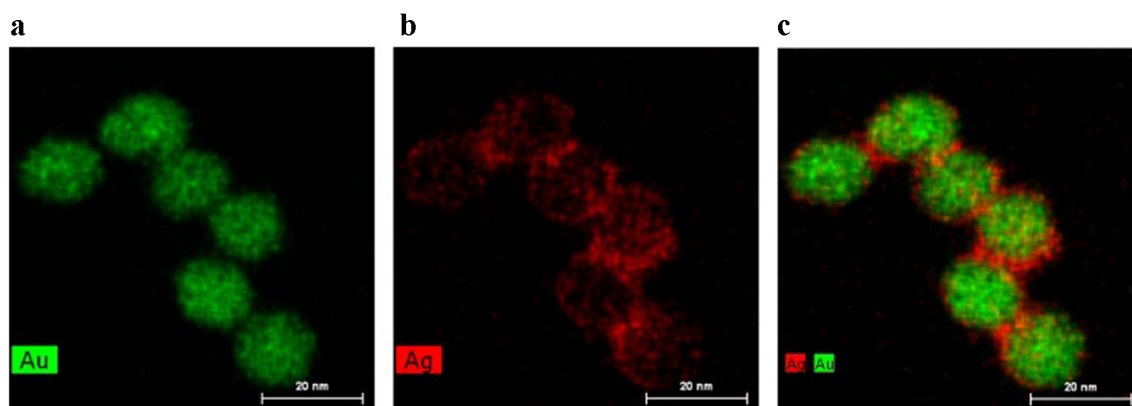
Fig. 2 The distribution of elements in Au@Ag #2 NPs obtained by EDS mapping: for Au (**a**), for Ag (**b**), and for combined distribution of Au and Ag (**c**)

provides precise control over not only composition and uniform spreading of Pt atoms but also morphology invariant (using Au@Ag #1–3 as the templates) and variant (using Au@Ag #4–6 as the templates) approaches for the manipulation of the optical properties (Fig. S11d), which can be further used for highly sensitive and multiplex bioanalysis [25, 26].

EDS was used for the study of the distribution of metals in NPs (Fig. 4). The results of the mapping show uniform distribution of Pt atoms across NPs (Fig. 4a, Fig. S12, 13). Au atoms do not participate in the galvanic replacement reaction and remain concentrated in the core area of NPs (Fig. 4b). The results of EDS demonstrate the presence of all three metals in Au@Ag #2–Pt #4 NPs. Chemical mapping of NPs confirms the uniform distribution (both in Ag shell areas and in the middle of NPs) of Pt atoms (Fig. S14). Because of the low concentration of Pt and its uniform distribution in the NPs, its characteristics' peaks have low intensity (Fig. 4c, Fig. S12). The relative contents of Au, Ag, and Pt were equal to 63.7, 23.0, and 13.3%.

For further developments, we focused on the Au@Ag #2 NPs and on the NPs obtained by galvanic replacement from them. The choice was determined by the relatively low Ag concentration, which facilitates the formation of Au@Ag-Pt NPs with the low load of Pt. The low consumption of the precious Pt precursor for the production of nanozymes with high PMA is highly desirable for practical use.

In the proposed method, the deposition of platinum achieved by galvanic replacement facilitates the formation of the dispersed catalytic sites on the surface of NPs. The conventional methods of Pt coating by the reduction of precursors result in Volmer-Weber growth (i.e., growth of Pt islands on the surface rather than covering) on Au and Ag substrates [27, 28] which are not efficient for catalysis because of the high fraction of the buried platinum atoms [29]. Compared with layer-by-layer growth, where precise control over diffusion and deposition rates is required, the developed approach's driving force (difference in standard reduction potentials) provides an easy, rapid, and reproducible synthesis procedure.

Peroxidase-mimicking activity of nanoparticles

PMA was monitored by oxidation of TMB with H_2O_2 in the presence of Au@Ag #2–Pt #4 NPs (Fig. S15 a, b). Specific activity (SA) was calculated to mg of Au because Au NPs do not participate in the galvanic replacement reaction, and the deposition of Ag and Pt occurs on only Au NPs. Neither Au NP nor Au@Ag #1–6 NPs demonstrated PMA.
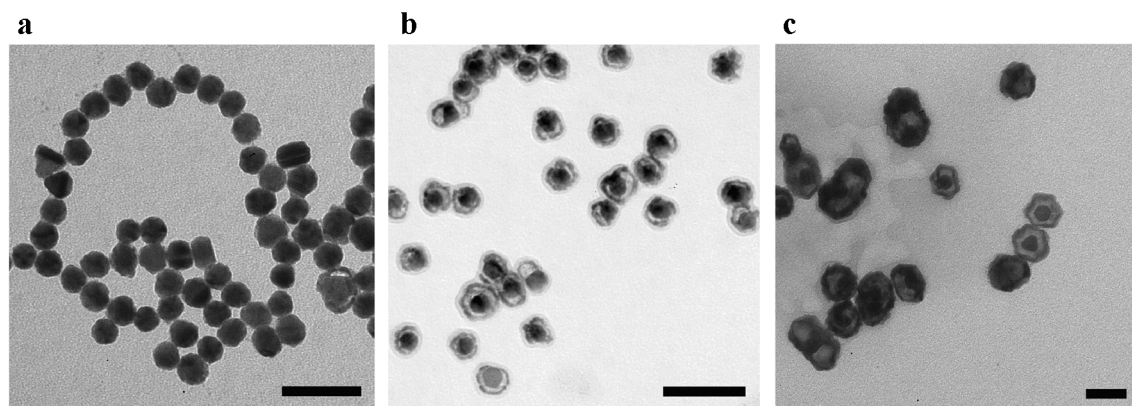
Fig. 3 Characteristics of NPs synthesized by galvanic replacement. TEM microphotographs of Au@Ag #2–Pt #4 NPs (**a**), Au@Ag #4–Pt #4 NPs (**b**), and Au@Ag #6–Pt NPs (**c**). The scale bar is equal to 50 nm
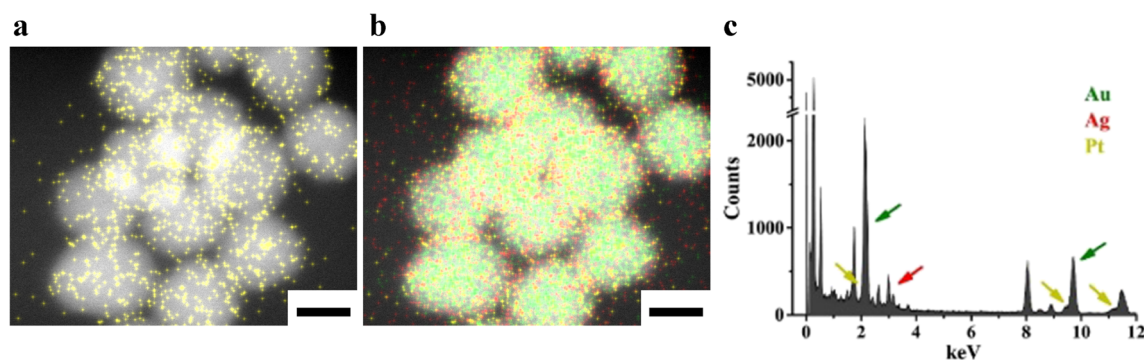
Fig. 4 Distribution of elements in Au@Ag #2–Pt #4 NPs obtained by high-angle annular dark-field microscopy combined with EDS mapping: for Pt (yellow) (**a**), for Au (green), Ag (red), and Pt (yellow) (**b**). The scale bar is equal to 10 nm. EDX spectra of NPs: peaks of elements are shown with colored arrows; Lα and Lβ lines were registered (**c**)

Km values measured were equal to 0.06 mM for TMB and 320 mM for H_2O_2. However, as shown in the review by Wu et al. [30], the reported values of kinetic constants for various Pt-containing nanozymes are varied in a broad range (up to 2–3 folds). For the precise comparison of the PMA of nanozymes, the SA values can be used [31]. The SA values for Au@Ag #2–Pt #1–7 NPs were calculated (SA values are summarized in Table S3). NPs synthesized in excess of Pt over the predicted load (i.e., $Pt^{4+}/Ag > 1$) demonstrated comparable SA values (Fig. S15c, Table S4). This observation also proves the deposition of Pt is performed only by the galvanic replacement of Ag in NPs and PMA is determined by the amount of Pt atoms. Hence, Au@Ag #2–Pt #1–3 NPs are synthesized in the high concentration of Pt precursor; their SA is determined by the deposited in NP concentration of Pt, which is related to the concentration of Ag. Thus, the SA values of Au@Ag-Pt NPs can be regulated by changing the Ag precursor concentration during the synthesis of Au@Ag NPs and by the Pt precursor concentration during galvanic replacement.

To demonstrate the benefits of the developed approach, the Au@Ag#2-Pt NPs were compared in SA values with core@shell Au@Pt NPs. The Au@Pt NPs were synthesized by the reduction of Na_2PtCl_6 in the presence of Au NPs (S 1.4. Synthesis of Au@Pt nanoparticles). The Au@Ag-Pt nanozymes demonstrated 35–85 times higher SA values in comparison with the Au@Pt nanoparticles with the same Pt content (Fig. S16).

The SA value of Au@Ag #2–Pt #4 NPs was about 80% compared to Au@Ag #2–Pt #1–4 NPs. However, the synthesis of Au@Ag #2–Pt #4 NPs required 2–8 times lower consumption of Pt precursor in comparison with Au@Ag #2–Pt #1–3 NPs. Considering the balance of Pt precursor consumption and PMA, we selected Au@Ag #2–Pt #4 NPs for further use as the label for LFIA.

Conjugation of nanoparticles with antibodies, optimization of lateral flow immunoassay

Conjugation of mAb with NPs was performed by physical adsorption which ensures the synthesis of highly stable conjugates and retains antigen-binding properties of adsorbed mAb [32]. The concentrations of mAb for the conjugation with NPs were selected using the flocculation curves method, which determines the stability of conjugates in the solution with high ionic strength. Coating NPs with mAb prevents particles' aggregation controlled by NPs' absorbance spectrum (Fig. S17). For the conjugation with NPs, the concentrations of mAb exceeding the minimal stabilized concentration (concentrations of mAb at which the curve reaches the plateau) at 30% were used (Fig. S18). These included 12, 11, and 10 μg mL^{-1} for Au NPs, Au@Ag NPs, and Au@Ag #2–Pt #4 NPs, respectively. The lower concentration of mAb was used for the conjugation with Au@Ag #2–Pt #4 NPs to avoid dense coverage of the surface of NPs that may cause the reduction of PMA [33].

Adsorption of mAb on the surface of NPs results in the increase of hydrodynamic diameters from 23.5 ± 5.6 to 50.1 ± 13.1 nm for Au NPs and their conjugate with mAb (Fig. S19 a), from 27.4 ± 8.8 to 69.0 ± 24.4 nm for Au@Ag #2 NPs and their conjugate with mAb (Fig. S19 b), and from 36.3 ± 9.0 to 80.7 ± 36.6 nm for Au@Ag #2–Pt #4 NPs and their conjugate with mAb (Fig. S19 c).

The concentration of mAb conjugated to Au@Ag #2–Pt #4 NPs was determined by ELISA (Fig. S20) as the difference between the concentrations of added and detected biotinylated mAb in the supernatant after conjugation. The results show all three types of NPs bound about 80% of added mAb. Synthesized conjugates were stable, and no aggregates were observed (Fig. S19). The conditions that provide the highest colorimetric signal (C2cc clone immobilized in TZ, C6cc clone conjugated to NPs, Fig. S21) were used in all further experiments.

Application of nanoparticles as the colorimetric and catalytic labels in lateral flow immunoassay

NPs act as the labels in LFIA, providing visual detection of immunocomplexes in TZ and CZ (Fig. 5a–c). Conjugates of mAb with NPs were used as the colorimetric (LFIA-1–3) and

catalytic label (LFIA-4). Au NPs were used as the conventional label in LFIA. Au@Ag #2–Pt #4 NPs were selected as the catalytic label based on the balance between low consumption of Pt precursor during synthesis and relatively high PMA. The comparison of LOD values between LFIA-1–3 will facilitate the estimation of the impact of the NPs' optical properties. The comparison of LOD values between LFIA-3 and LFIA-4 will facilitate the estimation of the impact of the catalytic properties of Au@Ag #2–Pt #4 NPs. The visual detection of qualitative results (i.e., presence or absence of visible coloration of TZ) for all four formats of LFIA facilitates equipment-free detection of CRP. The instrumental detection (i.e., quantitative measurement of coloration intensity in a grayscale mode, section S3) provides the accurate signal value regardless of its color (red for LFIA-1, dark-blue for LFIA-4).

The LOD values were equal to 3.9 ng mL^{-1} for LFIA-2 (Fig. 5e, plot II), 980 pg mL^{-1} for LFIA-1 and LFIA-3 (Fig. 5e, plots I and III), and 15 pg mL^{-1} for LFIA-4 (Fig. 5f, g). The higher LOD value for LFIA-2 could be explained by the similar coloration of Au@Ag NPs with serum. Thus, visual

and instrumental detection is hindered by staining the membrane with the sample (Fig. 5b). Red- and violet-colored Au and Au@Ag-Pt NPs (Fig. 5a, c) form contrasting TZs and CZs and could be detected simply visually and instrumentally. Because of the similar optical properties of Au and Au@Ag-Pt NPs, the decrease of LOD values was not achieved, and the colorimetric signal of TZs demonstrated the comparable values (Fig. 5e, plots I and III).

The use of PMA of Au@Ag-Pt NPs facilitates the significant increase of the colorimetric signals in TZs and CZs achieved by the accumulation of the dark-colored insoluble product of DAB oxidation. An optimization study showed a 5-min incubation of the substrate on the test strip provides high amplification of the colorimetric signal and the absence of nonspecific staining (Fig. S22). The LOD value of LFIA-4 was about 65 times lower in comparison with LFIA 1 and 3. In the case of LFIA-4, background staining (colorimetric signal ≈ 3 RU) was observed, and was not substantially reduced by post-assay washing of the test strips (Fig. S23). However, instrumental detection of colorimetric signal excludes the

Fig. 5 LFIA of CRP in serum using different NPs as the labels. The test strips after LFIA-1 (a), LFIA-2 (b), LFIA-3 (c), and LFIA-4 (d). The numbers above the test strips correspond to the concentration of CRP, ng mL^{-1}: 1 – 1000, 2 – 500, 3 – 250, 4 – 125, 5 – 62.5, 6 – 31.2, 7 – 15.6, 8 – 7.8, 9 – 3.9, 10 – 1.9, 11 – 0.98, 12 – 0.49, 13 – 0.244, and 14 – 0.122; concentration of CRP, pg mL^{-1}, 15 – 61, 16 – 30, 17 – 15, and 18 – 7; and 0 – blank probe. Calibration curves for: LFIA-1 (I), LFIA-2 (II), and LFIA-3 (III) (e), LFIA-4 (f). Plot at low CRP concentrations. The black-dotted line corresponds to the background (g)
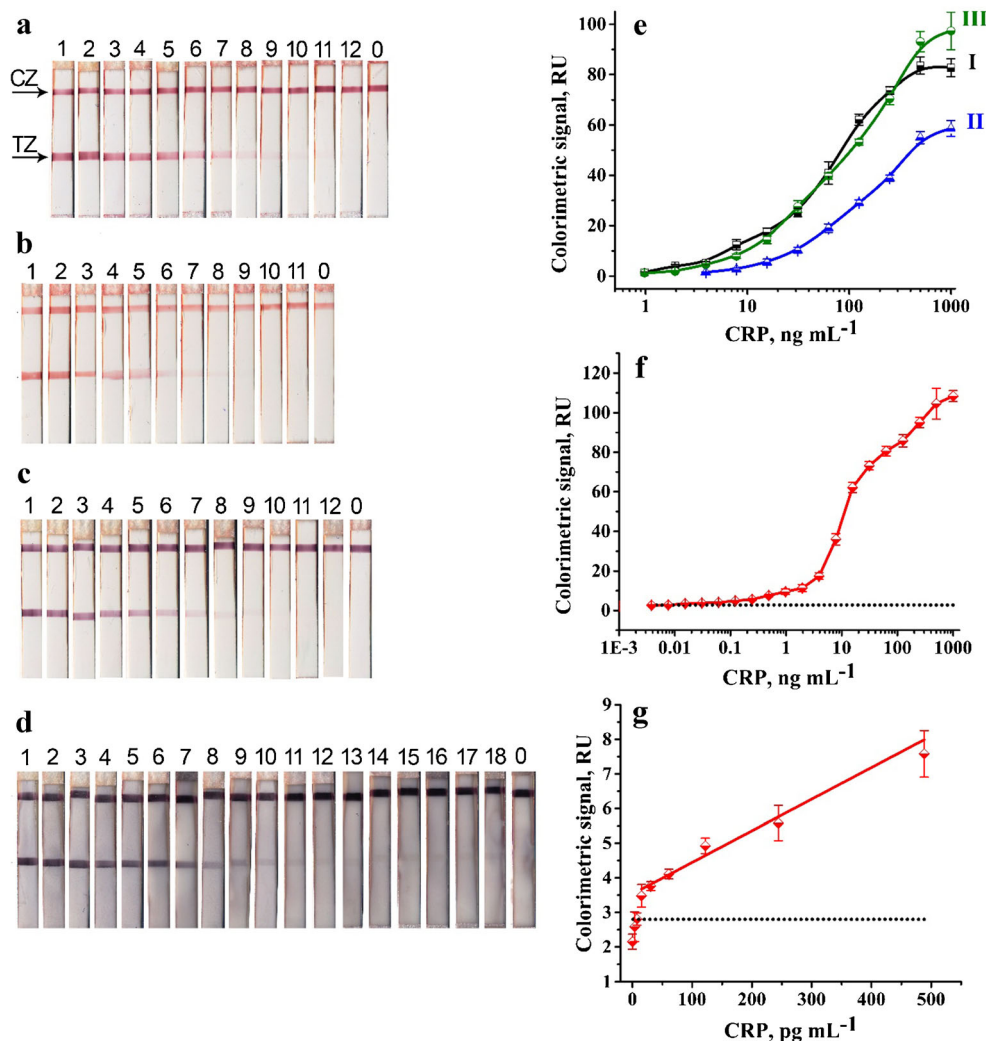
impact of the background staining (black-dotted line on Fig. 5g) and facilitate the reliable detection of CRP at such low concentrations as 15 pg mL^{-1} (Fig. 5g). The sample preparation included dilution of serum samples. The consistency of the steps for preparation of spiked serum (i.e., spiking CRP in undiluted serum and dilution with PBST or dilution with PBST and then spiking with CRP) does not influence the colorimetric signal (Fig. S24).

Previously published articles describing the use of Pt-containing nanozymes report the decrease of LOD values in the range of 10 to 2000 times (Table S5). However, in the developed method, the consumption of precious Pt precursors was significantly lower (2–200 times), and comparable LOD reduction was achieved (Table S5). Thus, the higher utilization of surface-dispersed Pt catalytic centers facilitates high signal amplification and low consumption of costly precursors.

Although LFIA of CRP with comparable LODs were reported (50 pg mL^{-1} for LFIA with mesoporous SiO$_2$ coated up-converting nanoparticles [34]; 10 pg mL^{-1} for LFIA with Raman reporter-embedded Au@Ag NPs [35]), the proposed here LFIA-4 can be performed without additional equipment and with visually estimated coloration of TZ and CZ. Compared with other earlier described equipment-free LFIA for CRP, the proposed in this work LFIA-4 provides rapid and convenient point-of-need detection with the lowest LOD value (Table S6).

Among the alternative method of CRP detection, electrochemical and fluorescence methods are actively developed [36, 37]. Although fluorescent methods facilitate nanomolar LOD of CRP [37], the requirements for sophisticated equipment usually restrict the use of these methods only for laboratories. Electrochemical methods facilitate detection with the range of nano-picogram LOD (Table S7). Despite their high sensitivity, the reported electrochemical methods are instrumental and are more time-consuming (40–60 min) as compared to LFIA. The developed LFIA combines the benefits of the point-of-care method (rapidity, easy-to-operate, low cost, and equipment-free procedure) with high sensitivity. The LOD value of the developed LFIA is comparable with the values reported for electrochemical (i.e., 3.3–15 pg mL^{-1}) [38–40] and ELISA-like procedure with nanozymes (8pg mL^{-1}) [41].

The drawback of the LFIA-4 is the necessity of the additional substrate addition stage, which increases the assay time. The further development of a test system with a dried substrate will make this approach more convenient for practice [42]. Despite this additional stage, LFIA-4 preserves the benefits of the rapid point-of-care method (total assay time within 10 min).

Validation of lateral flow immunoassay on real samples

The used clones of mAb did not react with non-target serum proteins (Fig. S25). LFIA-3 and LFIA-4 detect specifically CRP; no coloration of TZs was observed even at high concentrations of non-target abundant human serum proteins (immunoglobulins and human serum albumin, Fig. S26) and others cardiac or inflammation biomarkers (procalcitonin, cardiac troponins I and T).

LFIA-3 and LFIA-4 were validated on real samples of human plasma, serum, and capillary blood. The accuracy of LFIA-3 and LFIA-4 was evaluated by the recovery studies of spiked rabbit serum (Fig. S27) and the correlation of the quantitative results with ELISA in diluted human plasma (Fig. S28).

The sample of rabbit serum does not contain CRP and thus facilitates the establishment of the quantitative characteristics of the LFIA's recovery. The samples of rabbit serum were spiked with the different CRP concentrations, and then the recovery percent (measured CRP concentration/spiked CRP concentration * 100%) was determined. The concentration range of CRP (i.e., the concentration of spiked CRP) for the recovery studies was selected based on the clinical-relevant concentrations of CRP for healthy people (< 3 μg mL^{-1}) and up to 200–400 μg mL^{-1} for patients with bacterial infections and inflammations [43, 44]. Thus, considering the dilution of the samples for LFIA, the usefulness of the highly sensitive CRP detection for the evaluation of cardiovascular diseases risk [45], and the request for the less invasive sample collection procedures [46] (i.e., collection of small volumes of samples and further dilutions with buffers), we were focused on the range of low concentrations of CRP (1–20 ng mL^{-1}). Recovery studies demonstrated a recovery range of 86.6–117.0% for LFIA-3 (correlation coefficient between added and measured CRP is equal to $R^2 = 0.967$) and of 83.7–116.2% for LFIA-4 (correlation coefficient between added and measured CRP is equal to $R^2 = 0.987$).

Then, we determined the correlation coefficients between CRP concentrations in human plasma samples measured by LFIA and ELISA. The human plasma naturally contains CRP in the range 3–20 μg mL^{-1}. The dilutions of the plasma were selected based on the above range of CRP concentrations. The quantitative results of CRP concentrations in dilutions of the plasma samples were compared. The quantitative results of LFIA-3 and LFIA-4 demonstrated high correlation with ELISA ($R^2 = 0.99$ for LFIA-3, and $R^2 = 0.986$ for LFIA-4, Fig. S28). No false-positive and false-negative results were observed.

Because of the assay's high sensitivity, a small amount of the sample may be collected and diluted by buffer solutions to the volumes required for the assay (70–100 μL). Considering the significant increase of CRP levels during severe infections and sepsis [47] and the high sensitivity of LFIA-4, the ultra-low volume of the sample is required (≈ 0.2 μL of biological sample diluted to 100 μL of buffer) for the reliable detection of clinically relevant concentrations of CRP. This provides the possibility of performing LFIA-4 using capillary blood

(section S2). The collection of the capillary blood is an easy less traumatic procedure (compared to vein blood collection) and rapid (less than 1 min) procedure, which can be done in the point-of-care testing by a user without medical training (i.e., using a conventional lancet pen device).

The preliminary results demonstrated the applicability of LFIA-4 for the detection of CRP in capillary blood (Fig. S29). For capillary blood samples 5–7, the colorimetric signal of TZ for LFIA-3 and LFIA-4 demonstrated close values that can be explained by the high background staining of the test strips and therefore the lower value of the signal-to-noise ratio. The growth of the background is explained by the presence of nonenzymatic compounds with PMA (i.e., hemoglobin, which arises from the hemolysis of erythrocytes during blood collection, as well as other Fe-containing proteins) [48]. The elimination of the background will require the further optimization of the assay parameters. For capillary blood samples 1, 2, 3, and 8, LFIA-4 demonstrated a significant increase of the colorimetric signal (up to 12 times) in comparison with LFIA-1 and facilitated the conventional visual detection of the more contrasted TZs. Samples 4 and 9 demonstrated false-negative results obtained by LFIA-1 and LFIA-3, whereas LFIA-4 showed visually and instrumentally distinguished coloration of TZ (Fig. S29).

Conclusion

Trimetallic nanozyme consisting of Au core, Ag shell, and the surface-exposed Pt atoms (Au@Ag-Pt) were synthesized. Uniform distribution of Pt on the surface of the nanozyme facilitates high metal utilization and boosts the particles' peroxidase-mimicking activity.

The limit of the detection of C-reactive protein was reduced to 15 pg mL^{-1}: the lowest among equipment-free colorimetric lateral flow immunoassays. The developed lateral flow immunoassay showed absolute specificity and sensitivity for the detection of C-reactive protein in serum, plasma, and capillary blood. Because of its high sensitivity, the assay requires a small amount of the sample (0.1 μL) and may be used for self-testing by unskilled persons. The authors considered the further development of this point-of-care test by coupling it with dried blood spots approach that will make the whole procedure easier and more applicable for use in resource-limited settings.

Declarations

Conflict of interest The authors declare no competing interests.

References

1. Jin S, Wu C, Ye Z, Ying Y (2019) Designed inorganic nanomaterials for intrinsic peroxidase mimics: a review. Sensors Actuators B Chem 283:18–34. https://doi.org/10.1016/j.snb.2018.10.040

2. Yang H, He Q, Chen Y, Shen D, Xiao H, Eremin SA, Cui X, Zhao S (2020) Platinum nanoflowers with peroxidase-like property in a dual immunoassay for dehydroepiandrosterone. Microchim Acta 187:592. https://doi.org/10.1007/s00604-020-04528-9

3. Panferov VG, Safenkova IV, Zherdev AV, Dzantiev BB (2021) The steadfast Au@Pt soldier: peroxide-tolerant nanozyme for signal enhancement in lateral flow immunoassay of peroxidase-containing samples. Talanta 225:121961. https://doi.org/10.1016/j.talanta.2020.121961

4. Wei Z, Xi Z, Vlasov S, Ayala J, Xia X (2020) Nanocrystals of platinum-group metals as peroxidase mimics for in vitro diagnostics. Chem Commun 56:14962–14975. https://doi.org/10.1039/D0CC06575G

5. Lori O, Elbaz L (2020) Recent advances in synthesis and utilization of ultra-low loading of precious metal-based catalysts for fuel cells. ChemCatChem 12:3434–3446. https://doi.org/10.1002/cctc.202000001

6. Rodrigues TS, da Silva AGM, Camargo PHC (2019) Nanocatalysis by noble metal nanoparticles: controlled synthesis for the optimization and understanding of activities. J Mater Chem A 7:5857–5874. https://doi.org/10.1039/C9TA00074G

7. Casals NGE, Ojea I, Varon M, Puntes V (2012) The reactivity of colloidal inorganic nanoparticles. In: Hashim AA (ed) The delivery of nanoparticles. IntechOpen, London, pp 377–400. https://doi.org/10.5772/35238

8. Meng X, Zare I, Yan X, Fan K (2020) Protein-protected metal nanoclusters: an emerging ultra-small nanozyme. WIREs Nanomed Nanobiotechnol 12:1–21. https://doi.org/10.1002/wnan.1602

9. Yang T, Ahn J, Shi S et al (2021) Noble-metal nanoframes and their catalytic applications. Chem Rev 121:796–833. https://doi.org/10.1021/acs.chemrev.0c00940

10. Gao Z, Ye H, Tang D, Tao J, Habibi S, Minerick A, Tang D, Xia X (2017) Platinum-decorated gold nanoparticles with dual functionalities for ultrasensitive colorimetric in vitro diagnostics. Nano Lett 17:5572–5579. https://doi.org/10.1021/acs.nanolett.7b02385

11. Jiao L, Xu W, Wu Y, Yan H, Gu W, du D, Lin Y, Zhu C (2021) Single-atom catalysts boost signal amplification for biosensing. Chem Soc Rev 50:750–765. https://doi.org/10.1039/D0CS00367K

12. Ye H, Wang Q, Catalano M, Lu N, Vermeylen J, Kim MJ, Liu Y, Sun Y, Xia X (2016) Ru nanoframes with an fcc structure and enhanced catalytic properties. Nano Lett 16:2812–2817. https://doi.org/10.1021/acs.nanolett.6b00607

13. Xia X, Figueroa-Cosme L, Tao J, Peng HC, Niu G, Zhu Y, Xia Y (2014) Facile synthesis of iridium nanocrystals with well-controlled facets using seed-mediated growth. J Am Chem Soc 136:10878–10881. https://doi.org/10.1021/ja505716v

14. Bai T, Wang M, Cao M, Zhang J, Zhang K, Zhou P, Liu Z, Liu Y, Guo Z, Lu X (2018) Functionalized Au@Ag-Au nanoparticles as an optical and SERS dual probe for lateral flow sensing. Anal

Bioanal Chem 410:2291–2303. https://doi.org/10.1007/s00216-018-0850-z

15. da Silva AGM, Rodrigues TS, Haigh SJ, Camargo PHC (2017) Galvanic replacement reaction: recent developments for engineering metal nanostructures towards catalytic applications. Chem Commun 53:7135–7148. https://doi.org/10.1039/C7CC02352A

16. Russo L, Merkoçi F, Patarroyo J, Piella J, Merkoçi A, Bastús NG, Puntes V (2018) Time- and size-resolved plasmonic evolution with nm resolution of galvanic replacement reaction in AuAg nanoshells synthesis. Chem Mater 30:5098–5107. https://doi.org/10.1021/acs.chemmater.8b01488

17. Londono-Calderon A, Bahena D, Yacaman MJ (2016) Controlled synthesis of Au@AgAu yolk–shell cuboctahedra with well-defined facets. Langmuir 32:7572–7581. https://doi.org/10.1021/acs.langmuir.6b01888

18. Liu X, Astruc D (2017) From galvanic to anti-galvanic synthesis of bimetallic nanoparticles and applications in catalysis, sensing, and materials science. Adv Mater 29:1605305. https://doi.org/10.1002/adma.201605305

19. Huang D, Lin B, Song Y, Guan Z, Cheng J, Zhu Z, Yang C (2019) Staining traditional colloidal gold test strips with Pt nanoshell enables quantitative point-of-care testing with simple and portable pressure meter readout. ACS Appl Mater Interfaces 11:1800–1806. https://doi.org/10.1021/acsami.8b15562

20. Li J, Liu F, Zhu Z, Liu D, Chen X, Song Y, Zhou L, Yang C (2018) In situ Pt staining method for simple, stable, and sensitive pressure-based bioassays. ACS Appl Mater Interfaces 10:13390–13396. https://doi.org/10.1021/acsami.8b03567

21. Huang Y, Xu T, Wang W, Wen Y, Li K, Qian L, Zhang X, Liu G (2020) Lateral flow biosensors based on the use of micro- and nanomaterials: a review on recent developments. Microchim Acta 187:70. https://doi.org/10.1007/s00604-019-3822-x

22. Yang H, Xu W, Zhou Y (2019) Signal amplification in immunoassays by using noble metal nanoparticles: a review. Microchim Acta 186:859. https://doi.org/10.1007/s00604-019-3904-9

23. Vashist SK, Venkatesh AG, Marion Schneider E, Beaudoin C, Luppa PB, Luong JHT (2016) Bioanalytical advances in assays for C-reactive protein. Biotechnol Adv 34:272–290. https://doi.org/10.1016/j.biotechadv.2015.12.010

24. Russell SM, Alba-Patiño A, Barón E, Borges M, Gonzalez-Freire M, de la Rica R (2020) Biosensors for managing the COVID-19 cytokine storm: challenges ahead. ACS Sens 5:1506–1513. https://doi.org/10.1021/acssensors.0c00979

25. Gao Z, Shao S, Gao W, Tang D, Tang D, Zou S, Kim MJ, Xia X (2021) Morphology-invariant metallic nanoparticles with tunable plasmonic properties. ACS Nano 15:2428–2438. https://doi.org/10.1021/acsnano.0c06123

26. Anfossi L, Di Nardo F, Cavalera S et al (2018) Multiplex lateral flow immunoassay: an overview of strategies towards high-throughput point-of-need testing. Biosensors 9:2. https://doi.org/10.3390/bios9010002

27. Merkoçi F, Patarroyo J, Russo L, Piella J, Genç A, Arbiol J, Bastús NG, Puntes V (2020) Understanding galvanic replacement reactions: the case of Pt and Ag. Mater Today Adv 5:100037. https://doi.org/10.1016/j.mtadv.2019.100037

28. Gao Z, Tang D, Tang D, Niessner R, Knopp D (2015) Target-induced nanocatalyst deactivation facilitated by core@shell nanostructures for signal-amplified headspace-colorimetric assay of dissolved hydrogen sulfide. Anal Chem 87:10153–10160. https://doi.org/10.1021/acs.analchem.5b03008

29. González E, Merkoçi F, Arenal R, Arbiol J, Esteve J, Bastús NG, Puntes V (2016) Enhanced reactivity of high-index surface platinum hollow nanocrystals. J Mater Chem A 4:200–208. https://doi.org/10.1039/C5TA07504A

30. Wu J, Wang X, Wang Q, Lou Z, Li S, Zhu Y, Qin L, Wei H (2019) Nanomaterials with enzyme-like characteristics (nanozymes): next-generation artificial enzymes (II). Chem Soc Rev 48:1004–1076. https://doi.org/10.1039/C8CS00457A

31. Jiang B, Duan D, Gao L, Zhou M, Fan K, Tang Y, Xi J, Bi Y, Tong Z, Gao GF, Xie N, Tang A, Nie G, Liang M, Yan X (2018) Standardized assays for determining the catalytic activity and kinetics of peroxidase-like nanozymes. Nat Protoc 13:1506–1520. https://doi.org/10.1038/s41596-018-0001-1

32. Di Nardo F, Cavalera S, Baggiani C et al (2019) Direct vs mediated coupling of antibodies to gold nanoparticles: the case of salivary cortisol detection by lateral flow immunoassay. ACS Appl Mater Interfaces 11:32758–32768. https://doi.org/10.1021/acsami.9b11559

33. Loynachan CN, Thomas MR, Gray ER, Richards DA, Kim J, Miller BS, Brookes JC, Agarwal S, Chudasama V, McKendry RA, Stevens MM (2018) Platinum nanocatalyst amplification: redefining the gold standard for lateral flow immunoassays with ultrabroad dynamic range. ACS Nano 12:279–288. https://doi.org/10.1021/acsnano.7b06229

34. Guo J, Chen S, Tian S, Liu K, Ma X, Guo J (2021) A sensitive and quantitative prognosis of C-reactive protein at picogram level using mesoporous silica encapsulated core-shell up-conversion nanoparticle based lateral flow strip assay. Talanta 230:122335. https://doi.org/10.1016/j.talanta.2021.122335

35. Rong Z, Xiao R, Xing S, Xiong G, Yu Z, Wang L, Jia X, Wang K, Cong Y, Wang S (2018) SERS-based lateral flow assay for quantitative detection of C-reactive protein as an early bio-indicator of a radiation-induced inflammatory response in nonhuman primates. Analyst 143:2115–2121. https://doi.org/10.1039/C8AN00160J

36. Dhara K, Roy D (2020) Review on electrochemical sensing strategies for C-reactive protein and cardiac troponin I detection. Microchem J 156:104857. https://doi.org/10.1016/j.microc.2020.104857

37. Kokorina AA, Ponomaryova TS, Goryacheva IY (2021) Photoluminescence-based immunochemical methods for determination of C-reactive protein and procalcitonin. Talanta 224:121837. https://doi.org/10.1016/j.talanta.2020.121837

38. Ma Y, Yang J, Yang T, Deng Y, Gu M, Wang M, Hu R, Yang Y (2020) Electrochemical detection of C-reactive protein using functionalized iridium nanoparticles / graphene oxide as a tag. RCS Adv 10:9723–9729. https://doi.org/10.1039/c9ra10386d

39. Li B, Ge L, Lyu P, Chen M, Zhang X, Xie S, Wu Q, Kwok HF (2021) Handheld pH meter–assisted immunoassay for C-reactive protein using glucose oxidase–conjugated dendrimer loaded with platinum nanozymes. Microchim Acta 188:14. https://doi.org/10.1007/s00604-020-04687-9

40. Boonkaew S, Chaiyo S, Jampasa S, Rengpipat S, Siangproh W, Chailapakul O (2019) An origami paper-based electrochemical immunoassay for the C-reactive protein using a screen-printed carbon electrode modified with graphene and gold nanoparticles. Microchim Acta 186:153. https://doi.org/10.1007/s00604-019-3245-8

41. Xie J, Tang M-Q, Chen J, Zhu YH, Lei CB, He HW, Xu XH (2020) A sandwich ELISA-like detection of C-reactive protein in blood by citicoline-bovine serum albumin conjugate and aptamer-functionalized gold nanoparticles nanozyme. Talanta 217:121070. https://doi.org/10.1016/j.talanta.2020.121070

42. Panraksa Y, Apilux A, Jampasa S, Puthong S, Henry CS, Rengpipat S, Chailapakul O (2021) A facile one-step gold nanoparticles enhancement based on sequential patterned lateral flow immunoassay device for C-reactive protein detection. Sensors Actuators B Chem 329:129241. https://doi.org/10.1016/j.snb.2020.129241

43. Young B, Gleeson M, Cripps AW (1991) C-reactive protein: a critical review. Pathology 23:118–124

44. Kolb-Bachofen V (1991) A review on the biological properties of C- reactive protein. Immunobiol 183:133–145. https://doi.org/10.1016/S0171-2985(11)80193-2

45. Ledue TB, Rifai N (2003) Preanalytic and analytic sources of variations in C-reactive protein measurement : implications for cardiovascular disease risk assessment. Clin Chem 1271:1258–1271

46. Lei BUW, Prow TW (2019) A review of microsampling techniques and their social impact. Biomed Microdevices 21:81. https://doi.org/10.1007/s10544-019-0412-y

47. Castelli GP, Pognani C, Meisner M, Stuani A, Bellomi D, Sgarbi L (2004) Procalcitonin and C-reactive protein during systemic inflammatory response syndrome, sepsis and organ dysfunction. Crit Care 8:234–242. https://doi.org/10.1186/cc2877

48. Jiang B, Fang L, Wu K, Yan X, Fan K (2020) Ferritins as natural and artificial nanozymes for theranostics. Theranostics 10:687–706. https://doi.org/10.7150/thno.39827